

# Spectrally engineering photonic entanglement with a time lens

J. M. Donohue,<sup>1,\*</sup> M. Mastrovich,<sup>1,2</sup> and K. J. Resch<sup>1,†</sup>

<sup>1</sup>*Institute for Quantum Computing and Department of Physics & Astronomy,  
University of Waterloo, Waterloo, Ontario, Canada N2L 3G1*

<sup>2</sup>*Department of Physics, Harvey Mudd College, Claremont, California, USA 91711*

In the same manner that free-space propagation and curved glass lenses are used to shape the spatial properties of light, a combination of chromatic dispersion and devices known as *time lenses* may be used to reshape its temporal properties [1, 2]. These techniques have found extensive application in classical optical signal processing based on nonlinear optics [3–6]. A new set of challenges presents itself when processing quantum signals, including noise suppression and high fidelity requirements. In this work, we construct a single-photon time lens based on dispersion and nonlinear sum-frequency generation to image the spectral waveform of half of an entangled photon pair. We find that the joint spectrum of the photon pair has strongly negative frequency correlations before the time lens and strongly positive correlations afterwards, verifying that the process has an overall negative spectro-temporal magnification. The temporal imaging of energy-time entangled systems opens up a host of new possible techniques for distinctly quantum tasks in the frequency domain [7–9], including state engineering [10, 11], and our results demonstrate that the upconversion time lens is an essential part of the single-photon waveform manipulation toolkit.

To utilize photons in quantum communication and metrology, customized sources of single photons and precise control over their properties is necessary. The spectral, or energy-time, degrees of freedom are of particular interest as the information they carry is robust over long-distance fiber links [12]. Entanglement among these degrees of freedom is essential to applications such as high-dimensional quantum key distribution [9], nonlocal dispersion cancellation [7], and quantum-enhanced clock synchronization [8]. The nonlinear process of spontaneous parametric downconversion (SPDC), for example, provides a reliable source of energy-time entangled photons. Once created, control over the spectral waveforms of single photons is more difficult. Control over the spatial or polarization degrees of freedom can be accomplished with passive linear optics, but manipulating spectral waveforms requires more complex techniques such as fast electronic devices or nonlinear optical processes. Overcoming these challenges is essential for many quantum applications, such as interfacing with quantum memories [13], ultrafast photon switching [14], manipulating time-bin qubits [15], and temporal mode selection [16, 17]. Such control is also essential to engineer multiphoton spectral states with specific spectral correlations at wavelengths where properly phasematched materials do not exist [10, 11, 18, 19].

In this work, we demonstrate ultrafast control on quantum-optical waveforms with sub-picosecond features. We construct a temporal imaging system based on ultrafast nonlinear effects to manipulate the spectral profile of single photons. We apply this technique to half of an energy-time entangled pair produced with SPDC, and observe that the frequency anti-correlations are converted to positive correlations after the time lens. A

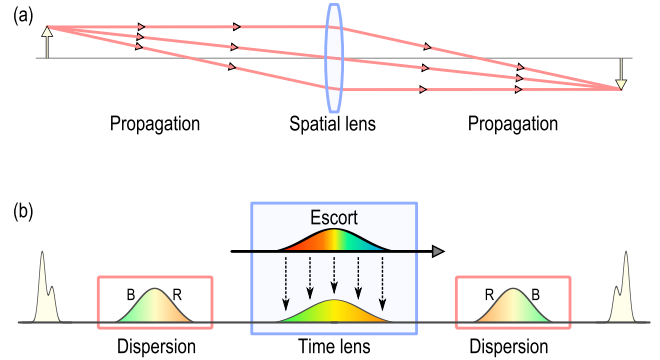


**FIG. 1. Temporal imaging with an upconversion time lens.** (a) In a spatial imaging system, free-space propagation spreads the spatial extent of the beam such that each portion of the beam has a distinct transverse momentum, visualized by the arrows. The lens shifts the momenta in a spatially dependent fashion, which effectively reverses the momenta for off-centre components and refocuses the beam with further spatial propagation. (b) The temporal imaging system operates through an analogous principle, where chromatic dispersion, such as encountered in optical fibre, spreads the temporal extent of the beam such that each temporal slice of the beam has a distinct central frequency, ranging from a red-shifted leading edge R to a blue-shifted tail B. The time lens introduces a time-dependent frequency shift, which can reverse the frequency shifts and allow the wavepacket to refocus itself after more chromatic dispersion is applied. If the pulse has temporal structure, it will be reversed akin to an imaging system with negative magnification. In our realization, we use sum-frequency generation with a dispersed escort pulse to implement an upconversion time lens. At each time in the interaction, the signal interacts with a different frequency of the escort, effectively enforcing a time-dependent relative frequency shift as well as a change in carrier frequency.

\* jdonohue@uwaterloo.ca

† kresch@iqc.ca

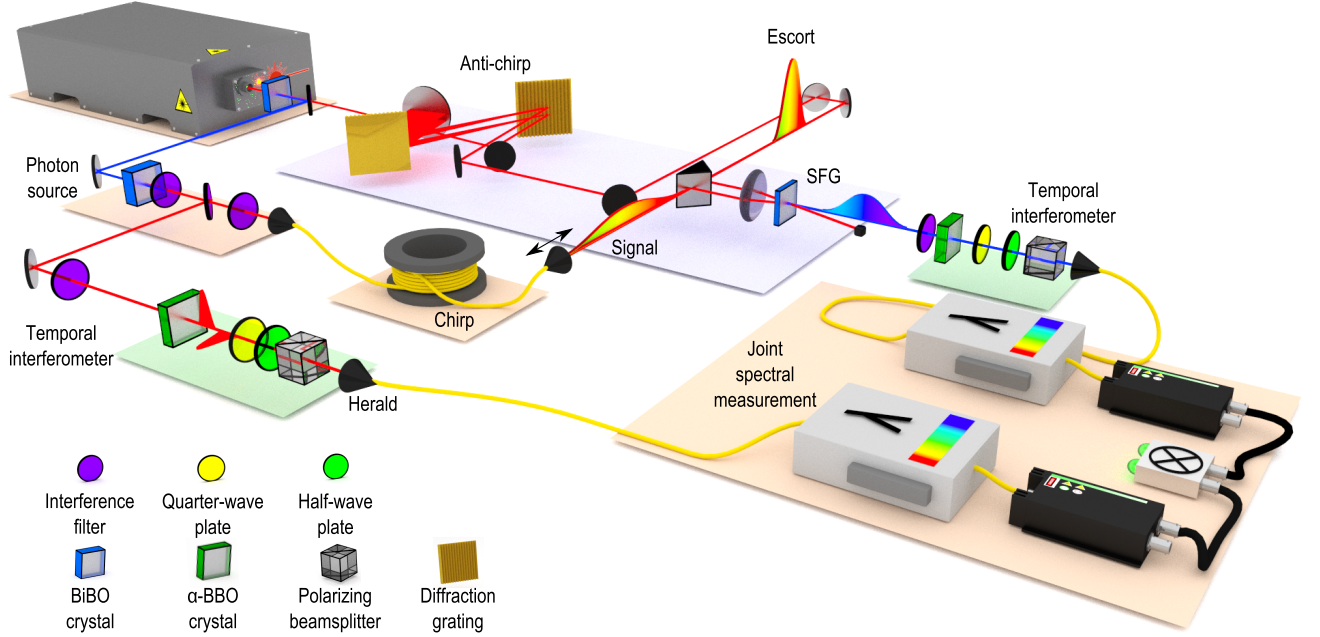


FIG. 2. **Experimental setup.** Frequency-entangled photons are created through the spontaneous parametric downconversion (SPDC) of ultrafast pulses from a Ti:Sapph laser frequency doubled via second harmonic generation (SHG). The signal photons are chirped with 34 m of single-mode fiber, while the remaining Ti:Sapph light is repurposed as the escort pulse and anti-chirped in a grating-based pulse compressor. The pulses are recombined for non-collinear sum-frequency generation (SFG), and the upconverted signal is cleaned with bandpass filters, coupled into multimode fiber, and spectrally resolved in coincidence with the herald. Wave-plates,  $\alpha$ -BBO crystals, and polarizing beamsplitters are used to measure two-photon temporal interference [20]. Full detail may be found in the methods section and supplemental material.

similar, as-yet-unrealized scheme was proposed by Tsang and Psaltis using electro-optic modulators [11]. We measure this correlation directly as a joint spectral intensity, and independently infer it from two-photon interference fringes [20, 21]. It is straightforward to adjust the temporal magnification by changing the chirp parameters, and our scheme is free of intense broadband noise such as Raman scattering.

Temporal imaging can be understood in direct analogy with its spatial counterpart [1, 2]. It is instructive to compare the corresponding elements in each, as shown in Fig. 1. In spatial imaging, free-space propagation causes the momentum components to diverge in space, resulting in a spatial spread of the beam. The action of the lens is to shift the transverse momenta in a spatially dependent way, such that after further propagation the beam may refocus. Analogously, in temporal imaging, propagation through a dispersive material (such as optical fiber) causes the constituent frequencies of a pulse to diverge in time, resulting in a temporal spread of the pulse. Constructing the equivalent of a lens for temporal imaging requires a time-dependent frequency shift in the same way that a spatial lens requires a spatially dependent transverse momentum shift. Fast electro-optics are effective for waveforms on the many-picosecond timescale [9], but all-optical nonlinear processes are required for waveforms with femtosecond timescales. Self-phase modulation can

be used in certain cases as well [2], but is ineffective for weak single-photon signals. Recent work has shown great promise using cross-phase modulation in photonic crystal fiber [22] and electro-optic modulators [23] to shape single-photon waveforms.

The upconversion time lens [4], seen in Fig. 1b, is based on sum-frequency generation (SFG), a type of three-wave mixing in which two pulses may combine to produce a pulse at the sum of their frequencies. In the case of interest, one pulse is considered to contain a single photon and the other to be a strong classical pulse. This strong classical pulse, referred to as the *escort*, upconverts the photon to a new frequency, leaving its own fingerprint on the spectral shape. SFG has been shown to be a powerful and potentially efficient tool for ultrafast waveform manipulation which remains effective at the single-photon level [12, 24–28]. The combination of SFG and pulse shaping has been shown to enable manipulation of ultrafast single-photon waveforms for techniques such as bandwidth compression [29], quantum pulse gates [16], and time-to-frequency conversion [5, 15].

We represent the spectral field of a dispersed optical pulse as  $F(\omega)e^{i\phi(\omega)}$ , where the spectral phase has a quadratic frequency dependence,  $\phi(\omega) = A(\omega - \omega_0)^2$ , with chirp parameter  $A$ . We characterize the dispersion applied to the input signal, escort pulse, and output waveform by the chirp parameters  $A_i$ ,  $A_e$ , and  $A_o$ ,

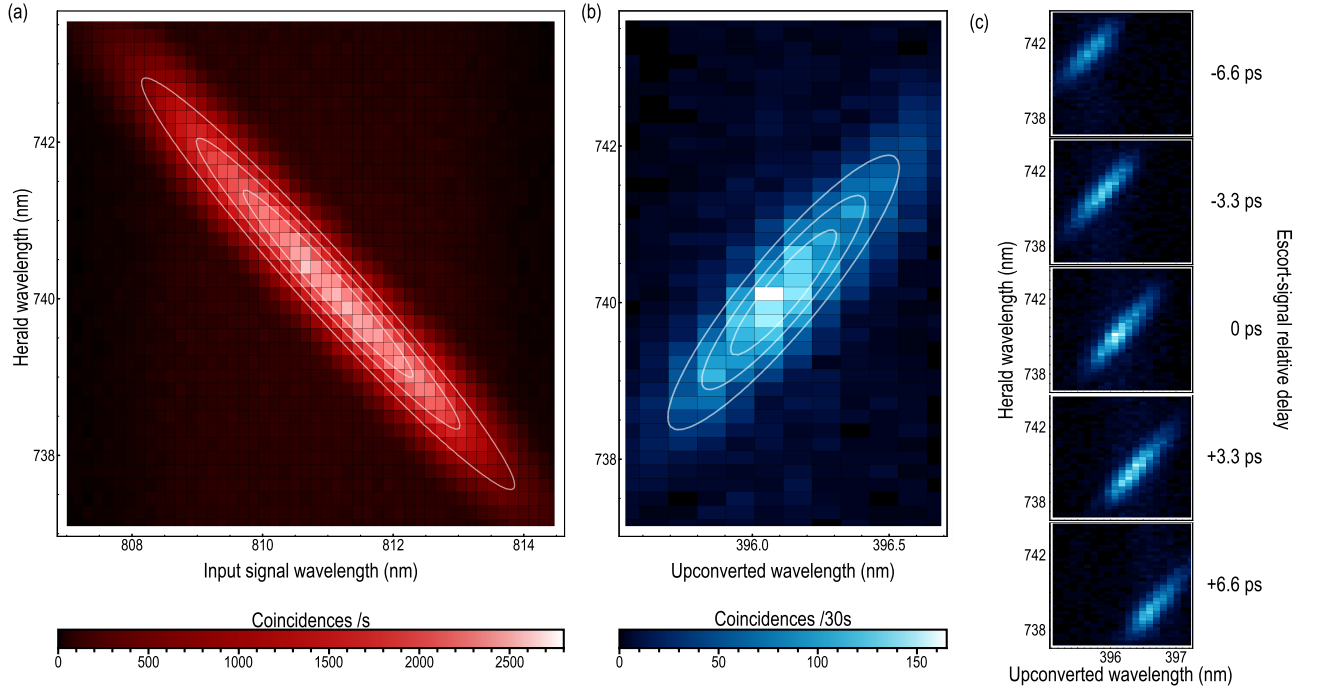


FIG. 3. **Joint Spectrum.** (a) The joint spectrum measured between the signal photon and the herald immediately after downconversion has strong frequency anti-correlations, exhibiting a statistical correlation of  $-0.9702 \pm 0.0002$  ( $-0.9776 \pm 0.0009$  when corrected for finite spectrometer resolution). (b) After sum-frequency generation, the joint spectrum between the upconverted signal photon and the herald exhibits strong positive frequency correlations, with a statistical correlation of  $+0.863 \pm 0.004$  ( $+0.909 \pm 0.005$  resolution-corrected). The white lines on each plot correspond to 25% contours of the resolution-corrected Gaussian fits. Background subtraction has not been employed in either image. (c) The center frequency of the joint spectrum is tunable by introducing a relative delay between the input signal and the escort pulse.

respectively, which in the case of normal dispersion are proportional to the length of material passed through. We assume that the pulses are all chirped to many times their initial widths, known as the large-chirp limit. In this limit, the imaging equation for the time lens system shown in Fig. 1b can be found in Refs. [4, 27] and simplifies to relation [2, 27],

$$\frac{1}{A_i} + \frac{1}{A_o} = -\frac{1}{A_e}. \quad (1)$$

This equation has the same form as the familiar thin lens equation, with dispersion taking the place of propagation distances and the escort chirp determining the temporal focal length.

In analogy to spatial imaging, the output temporal waveform will have the same features as the input but scaled by a magnification factor [2, 4, 27]

$$M_{\text{temporal}} = \frac{1}{M_{\text{spectral}}} = -\frac{A_o}{A_i} = \left(1 + \frac{A_i}{A_e}\right)^{-1}. \quad (2)$$

The inverse relations of the spectral and temporal magnification is a consequence of the scaling property of the Fourier transform. If  $A_i = -2A_e$ , the effective temporal and spectral magnification is  $-1$ , and both the temporal

and spectral shapes will be reversed. In the large-chirp limit, the output chirp  $A_o$  is all that is required to recompress the joint spectral state both spectrally and temporally. Note that the output chirp  $A_o$  has no effect on the spectral profile of the output. A derivation may be found in Supplementary Section II.

If the input signal is a single photon which is spectrally entangled with a partner, reversing the spectrum of the photon will result in an overall reversal of the two-photon joint spectrum. Using SPDC sources with extended phasematching conditions, joint spectra with positive spectral correlations have been produced before [18, 19, 30], but control over the correlations after state generation has not yet been demonstrated. This post-creation control is highly desirable for state engineering at wavelengths where suitably phasematched materials do not exist. Photon pairs with positively correlated spectra may be useful for dispersion cancellation in long-distance channels [19] and quantum-enhanced clock synchronization [8].

Our experimental setup is shown in Fig. 2, and is detailed in the Methods section. We create signal and herald photons through SPDC in 3-mm of bismuth borate (BiBO) stimulated by a pulsed laser. The downconverted photons are spectrally filtered and coupled into

single-mode (SM) fiber, from which they can each be sent to individual grating-based scanning spectrometers for spectral analysis, as seen in the initial joint spectrum of Fig. 3a. The signal photons can be instead sent through 34 m of SM fiber, where they are positively chirped by normal dispersion. The escort laser pulse passes through a grating-based compressor, set to apply half the dispersion as the fiber with the opposite sign [29]. The escort and signal photon are combined for SFG in 1-mm of BiBO, and the upconverted photon is measured with a third scanning spectrometer. The combined efficiency of the chirp, upconversion, and fiber coupling is approximately 0.2%. Detection events from the herald spectrometer were measured in coincidence with the upconverted photon spectrum, and the measured joint spectrum is shown in Fig. 3b. The output joint spectrum exhibits clear positive frequency correlations, in contrast with the clear anti-correlations seen in the input joint spectrum.

The measured joint spectra were then fit to a two-dimensional Gaussian. The spectrometers used had a spectral resolution of approximately 0.1 nm. While this resolution allowed us to resolve the essential spectral features, this finite resolution is on the same order of magnitude as our spectra, which artificially broadened their measured features. To account for the limited resolution, we deconvolved the fit spectra with a Gaussian spectrometer response function. The fit parameters of the joint spectra produced from our SPDC source and after SFG are shown in Fig. I. The statistical correlation  $\rho$  [10] both before and after the time lens is statistically significant, and the negative-to-positive change indicates the reversal of the correlations. By comparing the coincidences with the single-detection events before the spectrometers, we also calculate the second-order cross-correlation  $g_{s,h}^{(2)} = \frac{P_{s,h}}{P_s P_h}$  [13], where a value above two indicates non-classicality if we assume that the individual second-order statistics of the signal and herald are at most thermal (as expected for a pure single-photon state). The lower  $g_{s,h}^{(2)}$  value of the upconverted light can be attributed to the

Property	Input	Output
Signal bandwidth	$(11.56 \pm 0.02)$ THz	$(7.16 \pm 0.12)$ THz
Herald bandwidth	$(12.79 \pm 0.02)$ THz	$(8.51 \pm 0.13)$ THz
Correlation $\rho$	$-0.9776 \pm 0.0009$	$0.909 \pm 0.005$
$g_{s,h}^{(2)}$	$4.190 \pm 0.002$	$3.34 \pm 0.03$

TABLE I. **Joint spectral state parameters.** Selected properties of the Gaussian fits to the joint spectra seen in Fig. 3 are given above. The values are all corrected for the finite resolution of the spectrometers through deconvolution, and the widths are given full-width at half-maximum. The correlation parameters show that the spectral correlation is present after the time lens, but has changed from anti-correlation to positive correlation. The second-order cross-correlation  $g_{s,h}^{(2)}$  signifies nonclassical statistics with values greater than two, and was recorded before the spectrometers. A more extensive table of fit metrics can be found in the Supplementary Material.

spectrally distinguishable uncorrelated second-harmonic background which reaches the detectors. A more complete list of measured parameters, including other correlation quantifiers, may be found in Supplementary Section I.

Analogously to a laser beam incident off-centre to a lens, introducing a relative delay between the escort pulse and input signal results in a shift in the central wavelength of the joint spectrum, as shown in Fig. 3c. By tuning the relative delay over a range of  $\sim 13$  ps, the central frequency can be tuned over a range of  $\sim 11$  THz. However, it is also seen that the central wavelength of the herald changes as the delay is changed. This change in the herald implies that the upconversion time lens does not uniformly support the entire bandwidth of the input photon. As the escort pulse is less dispersed than the photon, as required for  $M = -1$  per Eq. (2), it does not fully envelope the input signal photon in time, analogous to a spatial lens with a clear aperture smaller than the input beam. This issue could be solved by using an escort pulse with a bandwidth significantly wider than the signal photon. Additionally, restrictions in the phase-matching of the upconversion medium will result in a narrowing of the upconverted signal spectra relative to the herald. These effects are detailed in Supplementary Section III.

As an independent measure of the spectral correlation of the upconverted signal, we measure two-photon interference using an ultrafast Franson-style interferometer [20, 21], as sketched in Fig. 4a. We use 2-mm birefringent  $\alpha$ -barium borate ( $\alpha$ -BBO) crystals at 45 degrees to split the upconverted signal and herald into two time bins with orthogonal polarizations separated by approximately 1.02 ps and 0.82 ps, respectively, where the difference is due to their wavelengths. We control the phase between the two bins with two waveplates and measure in superposition by projecting into linear polarization with a polarizing beam-splitter, as seen in Fig. 2 and Fig. 4a. The average visibility of the coincidence detection events seen in Fig. 4b is  $(15.6 \pm 1.0)\%$ , or  $(17.5 \pm 1.2)\%$  when background subtracted. In contrast, the visibility in the single-detection events in the upconverted and herald arms are, respectively,  $(0.4 \pm 0.4)\%$  and  $(0.06 \pm 0.04)\%$ . In Fig. 4c, it can be seen that the fringe phase depends on the difference of the two phases, which is indicative of spectral correlation, and Fig. 4b shows that this periodicity is only notable for the coincidence detections. See Supplementary Section IV for a full derivation of this effect with positive frequency correlations.

The correlations of the joint spectra and the nonlocal interference indicate entanglement so long as our two-photon state is nearly pure. While the visibility of the fringes in Fig. 4b contradicts a product state description for our system (i.e. a state of the form  $\rho_a \otimes \rho_b$ ), it is possible to describe with classical correlations. Previous experiments have established that photons created through SPDC are genuinely entangled rather than merely correlated [21] and that SFG maintains coherence [12, 15, 28].

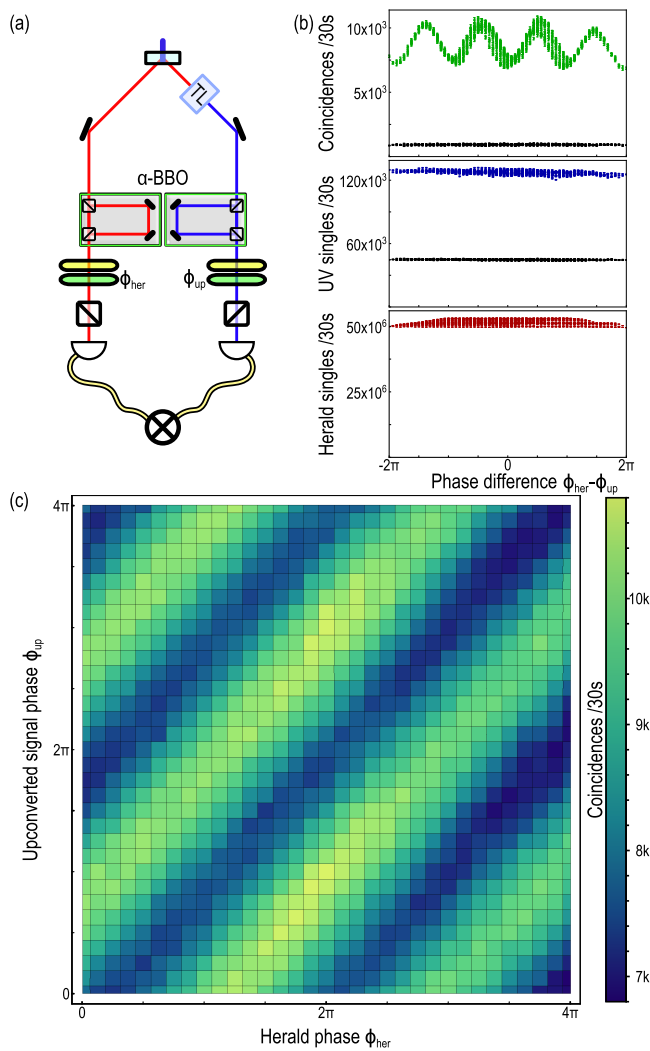


FIG. 4. **Two-photon interference fringes.** (a) The two-photon interferometer [20] produces interference fringes when two photons from a correlated source are split into early and late time bins and recombined with a phase applied to one bin. In our experiment, this interferometer was implemented on a picosecond timescale using short birefringent crystals ( $\alpha$ -BBO), waveplates, and polarizers, occurring after the time lens (TL) in the case of the signal. (b) The fringe visibility of the coincidences between the upconverted signal and herald viewed as a function of the phase difference display oscillations of  $(15.6 \pm 1.0)\%$  visibility, while the single-detection events of the upconverted photons and herald display are nearly flat with no discernable periodicity. Background counts obtained by blocking the input signal photon are shown in black. (c) A correlated interference pattern can be seen in the coincidences by the dependence of fringe oscillation on the difference of the two phases applied.

It would be possible to confirm genuine energy-time entanglement with additional temporal selection. However, the photon timescale in our experiment is on the order of hundreds of femtoseconds, which is well below the timing resolution of our detectors. This timescale is accessible,

however, with additional nonlinear processes [30].

We have shown control of an entangled twin-photon joint spectral intensity through the use of an upconversion time lens on the ultrafast timescale. The technique presented maintains two-photon correlations and introduces minimal background noise. The same components may also be used to form a general quantum temporal imaging system, capable of essential tasks such as bandwidth compression, time-to-frequency conversion, and all-optical transformations on time-bin encoded qubits. Control of the correlation of joint spectra as demonstrated here can be used to create two-photon states at wavelengths where efficient nonlinear materials with extended phasematching conditions do not exist [10, 18, 19, 30]. Such a technique may be directly useful for shaping the spectra of entangled pairs for long-distance communications, quantum-enhanced metrology [8], and more generally to mold the temporal distributions of single photons for experiments both fundamental and practical.

## METHODS

The experiment uses a titanium sapphire (Ti:Sapph) laser (Coherent Chameleon Ultra II, 80 MHz repetition rate). The fundamental of the Ti:Sapph was frequency-doubled in 2 mm of type-I phasematched bismuth borate (BiBO) to a second harmonic at  $(387.27 \pm 0.10)$  nm with a bandwidth of  $(0.75 \pm 0.04)$  nm full-width at half-maximum (FWHM). and a power of 935 mW. The photon pairs were then produced by focusing the second harmonic into 3 mm of type-I BiBO and split with a dichroic mirror, with central wavelengths of 811.0 nm and 740.2 nm for the signal and herald, respectively. For measuring two-photon interference, the herald passed through 2 mm of  $\alpha$ -barium borate ( $\alpha$ -BBO), a pair of wave-plates, and a polarizing beamsplitter (PBS) before being coupled into single-mode fiber.

The remaining Ti:Sapph fundamental is re-collimated and used as the escort pulse, which has a central wavelength of  $(774.6 \pm 0.4)$  nm with a bandwidth of  $(5.53 \pm 0.04)$  nm FWHM and a power of 945 mW. Part of the beam was split using a half-wave plate and PBS and delay-matched with the signal photon for alignment. The rest of the pulse passed through a double-pass grating-based pulse compressor which provides an anti chirp of  $A_e = -344 \times 10^3 \text{ fs}^2$  [29], with a razor blade inserted where the beam was at its widest to effectively act as an adjustable shortpass filter. The signal photon was chirped in 34 m of single-mode fiber, which provides a chirp of  $A_i = 696 \times 10^3 \text{ fs}^2$  through material dispersion. Owing to this fiber delay, the photon originates 13 pulses ahead of the escort. The chirped signal photon and anti-chirped escort pulse co-propagated with a spatial separation of approximately 9 mm and were then focused into 1 mm of type-I BiBO for sum-frequency generation. The upconverted beam, with a central wavelength of 396.1 nm, was then re-collimated and the second harmonic of the escort was removed with a pair of band-pass filters. The upconverted photons were then collected in multimode fiber after passing through a set of polarization optics identical to the herald photon. The herald photons are detected with Perkin-Elmer SPCM-AQ4C photon counting modules, with detection efficiencies of approximately 50%



near 800 nm. The upconverted photons were detected with Hamamatsu H10682-210 photon counters, with a quantum efficiency of approximately 30% near 400 nm. Coincidence counts were obtained with a window of 3 ns, which is larger than the timing jitter of the electronics and much smaller than the 12.5 ns pulse separation.

The joint spectra were measured using three scanning spectrometers, one for each of the near-infrared (NIR) SPDC photons and one for the upconverted photon. The beams were expanded to approximately 3.5 mm waist radius and directed to a grating for spectral separation (1200 lines/mm for NIR, 2400 lines/mm for ultraviolet). The beams were then focused onto a slit and multimode fiber coupler, which move together to measure the full spectrum. The resolution of spectrometers, measured using emission spectra of a calibration lamp, were found to be  $(0.136 \pm 0.013)$  nm,  $(0.148 \pm 0.012)$  nm, and  $(0.0741 \pm 0.0011)$  nm, for the NIR signal, NIR herald, and upconverted spectrometers, respectively.

The photons were produced through SPDC at a rate of approximately 415,000 coincidence counts per second, with  $2.5 \times 10^6$  ( $3.2 \times 10^6$ ) single-detection events per second for the signal (herald). After upconversion (but before the spec-

trometer), approximately 980 coincidence counts (7820 upconverted singles) per second were measured, with approximately 110 (2820) of those being background, of which the most significant source was the second harmonic of the escort pulse. This second harmonic background is spectrally resolvable from the upconverted photons, and thus does not have a significant effect on the joint spectral measurements.

A full-detail setup figure expanded from Fig. 2 may be found in Supplementary Section I.

## ACKNOWLEDGEMENTS

The authors would thank J. Lavoie, M. Karpiński, M. D. Mazurek, and K. A. G. Fisher for fruitful discussions, and C. Mastromattei for valuable assistance in the laboratory. We are grateful for financial support from the Natural Sciences and Engineering Research Council, the Canada Foundation for Innovation, Industry Canada, Canada Research Chairs, and the Ontario Ministry of Research and Innovation.

- 
- [1] Kolner, B. Space-time duality and the theory of temporal imaging. *IEEE J. Quantum Electron.* **30**, 1951–1963 (1994).
  - [2] Walmsley, I. A. & Dorrer, C. Characterization of ultrashort electromagnetic pulses. *Adv. Opt. Photon.* **1**, 308–437 (2009).
  - [3] Jopson, R., Gnauck, A. & Derosier, R. Compensation of fibre chromatic dispersion by spectral inversion. *IEEE Electron. Lett.* **29**, 576–578 (1993).
  - [4] Bennett, C. V., Scott, R. P. & Kolner, B. H. Temporal magnification and reversal of 100 Gb/s optical data with an up-conversion time microscope. *Appl. Phys. Lett.* **65**, 2513–2515 (1994).
  - [5] Foster, M. A. *et al.* Silicon-chip-based ultrafast optical oscilloscope. *Nature* **456**, 81–84 (2008).
  - [6] Foster, M. A. *et al.* Ultrafast waveform compression using a time-domain telescope. *Nat. Photon.* **3**, 581–585 (2009).
  - [7] Franson, J. Nonlocal cancellation of dispersion. *Physical Review A* **45**, 3126 (1992).
  - [8] Giovannetti, V., Lloyd, S. & Maccone, L. Quantum-enhanced positioning and clock synchronization. *Nature* **412**, 417–419 (2001).
  - [9] Nunn, J. *et al.* Large-alphabet time-frequency entangled quantum key distribution by means of time-to-frequency conversion. *Opt. Express* **21**, 15959–15973 (2013).
  - [10] Grice, W. P., U'Ren, A. B. & Walmsley, I. A. Eliminating frequency and space-time correlations in multiphoton states. *Phys. Rev. A* **64**, 063815 (2001).
  - [11] Tsang, M. & Psaltis, D. Propagation of temporal entanglement. *Phys. Rev. A* **73**, 013822 (2006).
  - [12] Tanzilli, S. *et al.* A photonic quantum information interface. *Nature (London)* **437**, 116–120 (2005).
  - [13] Albrecht, B., Farrera, P., Fernandez-Gonzalvo, X., Cristiani, M. & de Riedmatten, H. A waveguide frequency converter connecting rubidium-based quantum memories to the telecom C-band. *Nat. Commun.* **5** (2014).
  - [14] Hall, M. A., Altepeter, J. B. & Kumar, P. Ultrafast switching of photonic entanglement. *Phys. Rev. Lett.* **106**, 053901 (2011).
  - [15] Donohue, J. M., Agnew, M., Lavoie, J. & Resch, K. J. Coherent ultrafast measurement of time-bin encoded photons. *Phys. Rev. Lett.* **111**, 153602 (2013).
  - [16] Eckstein, A., Brecht, B. & Silberhorn, C. A quantum pulse gate based on spectrally engineered sum frequency generation. *Opt. Express* **19**, 13770–13778 (2011).
  - [17] Brecht, B., Reddy, D. V., Silberhorn, C. & Raymer, M. G. Photon temporal modes: A complete framework for quantum information science. *Phys. Rev. X* **5**, 041017 (2015).
  - [18] Eckstein, A., Christ, A., Mosley, P. J. & Silberhorn, C. Highly efficient single-pass source of pulsed single-mode twin beams of light. *Phys. Rev. Lett.* **106**, 013603 (2011).
  - [19] Lutz, T., Kolenderski, P. & Jennewein, T. Demonstration of spectral correlation control in a source of polarization-entangled photon pairs at telecom wavelength. *Opt. Lett.* **39**, 1481–1484 (2014).
  - [20] Franson, J. D. Bell inequality for position and time. *Phys. Rev. Lett.* **62**, 2205–2208 (1989).
  - [21] Kwiat, P. G., Steinberg, A. M. & Chiao, R. Y. High-visibility interference in a Bell-inequality experiment for energy and time. *Phys. Rev. A* **47**, R2472–R2475 (1993).
  - [22] Matsuda, N. Deterministic reshaping of single-photon spectra using cross-phase modulation. *Sci. Adv.* **2**, e1501223 (2016).
  - [23] Karpiński, M., Jachura, M., Wright, L. J. & Smith, B. J. Bandwidth manipulation of quantum light by an electro-optic time lens. *arXiv:1604.02459* (2016).

- [24] Huang, J. & Kumar, P. Observation of quantum frequency conversion. *Phys. Rev. Lett.* **68**, 2153–2156 (1992).
- [25] Vandevender, A. P. & Kwiat, P. G. High efficiency single photon detection via frequency up-conversion. *J. Mod. Opt.* **51**, 1433–1445 (2004).
- [26] Agha, I., Ates, S., Sapienza, L. & Srinivasan, K. Spectral broadening and shaping of nanosecond pulses: toward shaping of single photons from quantum emitters. *Opt. Lett.* **39**, 5677–5680 (2014).
- [27] Donohue, J. M., Mazurek, M. D. & Resch, K. J. Theory of high-efficiency sum-frequency generation for single-photon waveform conversion. *Phys. Rev. A* **91**, 033809 (2015).
- [28] Clemmen, S., Farsi, A., Ramelow, S. & Gaeta, A. L. Ramsey interference with single photons. *arXiv:1601.01105* (2016).
- [29] Lavoie, J., Donohue, J. M., Wright, L. G., Fedrizzi, A. & Resch, K. J. Spectral compression of single photons. *Nat. Photon.* **7**, 363–366 (2013).
- [30] Kuzucu, O., Wong, F. N., Kurimura, S. & Tovstionog, S. Joint temporal density measurements for two-photon state characterization. *Phys. Rev. Lett.* **101**, 153602 (2008).

## SUPPLEMENTARY MATERIAL

The supplementary material is organized as follows. Firstly, in Section I, we present a detailed experimental setup figure to supplement Fig. 2 of the main text and additional fit parameters of the measured joint spectra. In Section II, we flesh out the analogy between a spatial lens and a time lens. We then use a first-order perturbative method to model the upconversion time lens, and show how to extract the magnification factor. In Section III, we explore the effect of a relative time delay between the escort and the input signal, and show how it can be used to both adjust the center wavelength of the final signal and evaluate the effectiveness of the time lens itself. Finally, in Section IV, we derive the expected visibility in the nonlocal interferometer, and show the fringe pattern seen corresponds to a spectrally correlated state.

### I. ADDITIONAL EXPERIMENTAL DETAILS

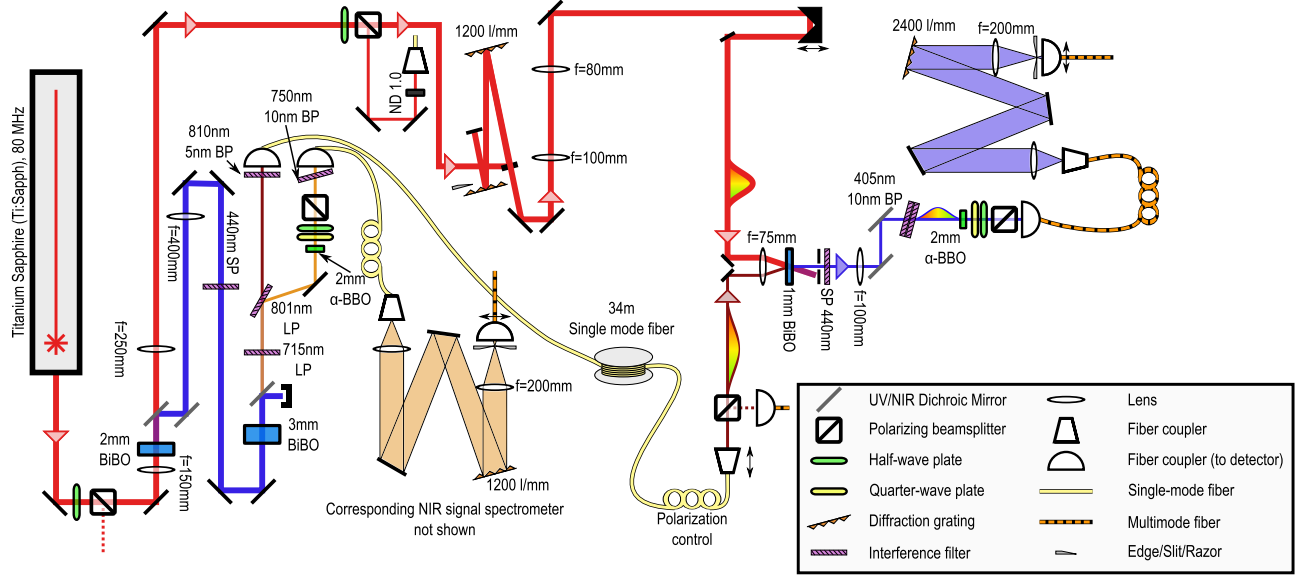


Figure S-1. **Full-detail experimental setup.** The experimental setup, as sketched in the main text, is more accurately represented as seen above. Filters can be longpass (LP), shortpass (SP), or bandpass (BP). Fiber loops with paddles are used to control polarization.

Property	Input		Output	
	Raw	Deconvolved	Raw	Deconvolved
Signal central wavelength	(811.006 ± 0.003) nm		(396.113 ± 0.004) nm	
Signal bandwidth	(4.047 ± 0.005) nm	(4.034 ± 0.006) nm	(0.621 ± 0.010) nm	(0.60 ± 0.01) nm
Herald central wavelength	(740.194 ± 0.003) nm		(740.126 ± 0.018) nm	
Herald bandwidth	(3.733 ± 0.005) nm	(3.716 ± 0.006) nm	(2.50 ± 0.04) nm	(2.47 ± 0.04) nm
Correlation $\rho$	-0.97024 ± 0.00015	-0.9776 ± 0.0009	0.863 ± 0.003	0.909 ± 0.005
Schmidt rank $K$	4.13 ± 0.01	4.75 ± 0.1	1.98 ± 0.03	2.39 ± 0.06
Joint energy uncertainty	(2.100 ± 0.006) THz	(2.092 ± 0.006) THz	(2.94 ± 0.05) THz	(2.86 ± 0.05) THz

TABLE S-I. **Complete fit joint spectral parameters.** Selected properties of the Gaussian fits to the joint spectra seen in Fig. 3 of the main text are given above. The deconvolved values are corrected for the finite resolution of the spectrometers used. All widths are reported full-width at half-maximum. We also calculate the Schmidt rank of the state under the assumption that the state is both pure and that any frequency-dependent phases do not affect the Schmidt decomposition, which is related to the statistical correlation as  $K = (1 - \rho^2)^{-1/2}$  from the purity of the partial trace. The joint energy uncertainty is defined as the width of the semi-minor axis of an elliptical Gaussian fit. The error bars are determined from Monte Carlo simulation of the data with the assumption of Poissonian count statistics.



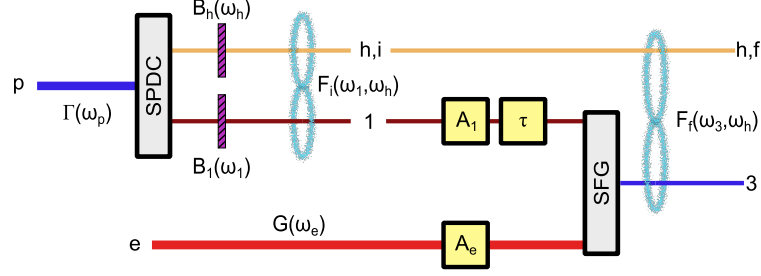


Figure S-2. **Abstract representation of setup.** The process under study begins with spontaneous parametric downconversion (SPDC) of a pump  $p$  with spectrum  $\Gamma(\omega_p)$ . The photon pair is filtered with bandpass filters  $B_j(\omega_j)$ . The photon pair, with a signal in mode 1 and a herald in mode  $h$ , share a joint spectral amplitude of  $F_i(\omega_1, \omega_h)$ . The signal is chirped, represented by the parameter  $A_1$ . An escort pulse in mode  $e$  with spectrum  $G(\omega_e)$  is also chirped, represented by the parameter  $A_e$ , as well as delayed in time relative to the input signal by an amount  $\tau$ . The signal photon and escort are mixed for sum-frequency generation (SFG), and the output joint spectral amplitude between the output signal in mode 3 and the herald is  $F_f(\omega_3, \omega_h)$ .

## II. DETAILED THEORETICAL DESCRIPTION

In this section, we explain the upconversion time lens. We first provide intuition for its operation by relating the quadratic phases of a spatial lens to those of dispersion and upconversion. We then tackle a Gaussian system with a first-order perturbative method. We consider solely the low-efficiency regime, where we can safely ignore effects of over-conversion and time-ordering [17, 27]. For ease of reference to subscripts and notation, see Fig. S-2.

### II.1. Contrasting a spatial lens and a time lens

As a Gaussian beam propagates in free space, its spatial distribution spreads out but its momentum distribution (given by the Fourier transform) remains constant. Solving the monochromatic paraxial Helmholtz equation, while ignoring  $y$ -dependence for simplicity, leads to the relation [1]

$$F(k_x, z) = F(k_x, 0)e^{i\frac{z}{2k_0}k_x^2}, \quad (S1)$$

where  $k_0 = n\omega_0/c$  is the  $z$ -momentum in the paraxial approximation. While the spatial intensity distribution  $f(x, z)$  expands, this quadratic phase does not change the distribution of transverse momenta,  $|F(k_x, z)|$ . As the beam propagates, the momentum components spread in space such that, in the large- $z$  limit, they each occupy a unique point; this spreading can therefore be thought of as a momentum-dependent spatial shift.

In contrast, a perfect parabolic lens in the thin-lens approximation imparts a phase that varies quadratically in space, transforming the spatial field to [1]

$$f(x, z) \mapsto f(x, z)e^{i\frac{k_0}{2f}x^2}, \quad (S2)$$

where  $f$  is the focal length. At the lens, the spatial profile does not change, but it does cause a spatially dependent momentum shift which allows for refocusing and manipulation of beams. We know [1, 2] that phases of this form lead to the thin lens equation,

$$\frac{1}{z_1} + \frac{1}{z_2} = \frac{1}{f}, \quad (S3)$$

with a magnification

$$M_{\text{spatial}} = -\frac{z_2}{z_1}. \quad (S4)$$

Since magnification of a Fourier transform obeys the scaling relationship  $\mathcal{F}[f(ax)] \propto F(k_x/a)$ , the magnification of the momentum distribution is simply  $1/M_{\text{spatial}}$ .

We next compare the treatment of a broadband pulse travelling as a plane wave through a medium. If we once again denote  $z$  as the propagation direction, the pulse centred about  $\omega_0$  will accumulate phase as

$$F(\omega, z) = F(\omega, 0)e^{ik(\omega)z} = F(\omega, 0)e^{ik_0z + ik'(\omega - \omega_0)z + i\frac{k''}{2}(\omega - \omega_0)^2z}, \quad (S5)$$

where we have expanded the wavevector  $k(\omega)$  to second order about the central frequency  $\omega_0$ . The first-order term corresponds to a time delay, while the second-order term corresponds to group velocity dispersion. In an analogous fashion as Eq. (S1), this quadratic phase will leave the intensity distribution in frequency  $|F(\omega)|$  unaltered, but will cause a frequency-dependent temporal shift. This leads to the creation of a chirped pulse, with the strength of chirp represented by the chirp parameter  $A$ , which is  $\frac{k''L}{2}$  for a medium of length  $L$ .

The missing piece of the puzzle is the temporal equivalent of a lens, an optic which implements the phase

$$f(t, z) \mapsto f(t, z)e^{iBt^2}, \quad (\text{S6})$$

where we can define a temporal focal length as  $f_t = \frac{\omega_0}{2B}$ . With this in place, we could write analogous thin-lens-type imaging equations as

$$\frac{1}{A_{in}} + \frac{1}{A_{out}} = 4B. \quad (\text{S7})$$

Some ways to impart the quadratic temporal phase include electro-optic modulators, self-phase modulation, sum-frequency generation, four-wave mixing, and cross-phase modulation [2]. Here, we briefly provide an intuitive picture for sum-frequency generation (SFG) with a chirped escort pulse [4]. In SFG, two pulses interact in a medium with a second-order nonlinearity. One pulse is treated as the weak input represented with the spectro-temporal amplitude  $f_i(t)$ , and the other as a strong undepleted escort pulse with amplitude  $g(t)$ . If the material is lossless and has a phasematching function much broader than the pulses in question, the upconverted temporal waveform in the low-efficiency regime will be given by [27]

$$f_f(t) \stackrel{\text{low-eff.}}{\propto} f_i(t)g(t). \quad (\text{S8})$$

If the escort pulse  $g(t)$  is a chirped Gaussian pulse with an envelope described by

$$G(\omega_e) = \frac{1}{(2\pi)^{1/4}\sqrt{\sigma_e}} \exp\left[-\frac{(\omega_e - \omega_{0e})^2}{4\sigma_e^2}\right] \exp\left[iA_e(\omega_e - \omega_{0e})^2\right], \quad (\text{S9})$$

then its temporal description can be written as

$$g(t) = \left(\frac{2}{\pi}\right)^{\frac{1}{4}} \sqrt{\frac{\sigma_e}{1 - 4iA_e\sigma_e^2}} \exp\left[-\frac{\sigma_e^2 t^2}{(1 + 16A_e^2\sigma_e^4)} - i\frac{4A_e\sigma_e^4 t^2}{1 + 16A_e^2\sigma_e^4}\right] = g'(t) \exp\left[-i\frac{4A_e\sigma_e^4 t^2}{1 + 16A_e^2\sigma_e^4}\right]. \quad (\text{S10})$$

If we look at the large-chirp limit (LCL), where the pulse is chirped to many times its initial width ( $A_e^2\sigma_e^4 \gg 1$ ), we can simplify the representation of the field to

$$g(t) \approx g'(t) \exp\left[-i\frac{t^2}{4A_e}\right]. \quad (\text{S11})$$

If we can also assume that the chirped escort pulse is much longer in time than the input, then  $|f_i(t)g(t)| \propto |f_i(t)|$  and the upconverted signal will only gain a phase (and central frequency shift) from the SFG process as

$$f_f(t) \propto f_i(t) \exp\left[-i\frac{t^2}{4A_e}\right]. \quad (\text{S12})$$

Thus, in these limits, SFG implements a temporal phase of  $B = -\frac{1}{4A_e}$ . Using this upconversion time lens, the imaging equations take the natural form

$$\frac{1}{A_i} + \frac{1}{A_o} = -\frac{1}{A_e}, \quad (\text{S13})$$

with a temporal magnification of

$$M_{\text{temporal}} = -\frac{A_o}{A_i} = \left(1 + \frac{A_i}{A_e}\right)^{-1}. \quad (\text{S14})$$

To obtain these, we had to assume freedom from phasematching and a sufficiently large chirp limit. Note that increasing the escort chirp decreases the effective focusing power of the time lens, but increases its temporal aperture. In the next section, we remove some of these simplifications and investigate our specific case more deeply.

A general imaging system requires more than a lens with free-space on either side. For magnifying beams, a full telescope is needed, which consists of at least two free-space propagation steps and two lens. Therefore, two time lens are needed for general reshaping of two-photon spectral states [6]. However, this can be relaxed in some limiting cases. We will see in the next section that the correlation reversal as shown in the main text can be done with one lens so long as we work in the large-chirp limit. The spatial equivalent of this scenario is working the limit such that the distance between the image plane and the lens is much greater than the transverse size of the beam. As the focal distance is increased, recollimation at the image plane after the lens has increasingly little effect. This large-chirp limit must be met in order for spectro-temporal reshaping to be effective with a single time lens, even if that time lens is idealized.

## II.2. First-order quantum sum-frequency generation with chirped pulses

We begin by describing the joint spectral state generated by SPDC in the low-gain regime post-selected for coincidences (i.e. a single photon pair) as

$$|\psi_i(t)\rangle = \frac{1}{2\pi} \iint d\omega_1 d\omega_h F_i(\omega_1, \omega_h) |\omega_1\rangle_1 |\omega_h\rangle_h, \quad (\text{S15})$$

where  $|\omega_j\rangle = \hat{a}_{\omega_j}^\dagger e^{i\omega_j t}|0\rangle$  represents a single photon of frequency  $\omega_j$  which is in a single spatial/polarization mode. The initial joint spectral representation  $F_i(\omega_1, \omega_h)$  is a function of the pump spectrum  $\Gamma(\omega_p)$ , the phasematching function  $\Phi_{SPDC}(\omega_1, \omega_h, \omega_p)$ , and any bandpass filters applied  $B_j(\omega_j)$  [10]. If we assume that each of these functions is individually well-approximated by a Gaussian, we can approximate the joint spectral wavefunction as approximated by a two-variable Gaussian,

$$F_i(\omega_1, \omega_h) = \Gamma(\omega_1 + \omega_h) \Phi_{SPDC}(\omega_1, \omega_h) B_1(\omega_1) B_h(\omega_h) \quad (S16)$$

$$= \frac{1}{\sqrt{2\pi\sigma_1\sigma_{h,i}(1-\rho_i^2)^{1/4}}} \exp \left[ \frac{1}{1-\rho_i^2} \left( -\frac{(\omega_1 - \omega_{01})^2}{4\sigma_1^2} - \frac{(\omega_h - \omega_{0h,i})^2}{4\sigma_{h,i}^2} - \frac{\rho_i(\omega_1 - \omega_{01})(\omega_h - \omega_{0h,i})}{2\sigma_1\sigma_{h,i}} \right) \right], \quad (S17)$$

where the simplified representation has been renormalized. Note that the single-photon marginal spectra in this model are symmetric about their central frequencies, with  $1/e$  widths of  $\sigma$ .

The signal photon is then chirped and delayed, which can be represented respectively as a quadratic and linear phase in frequency as

$$F_i(\omega_1, \omega_h) \mapsto F_i(\omega_1, \omega_h) e^{-i\omega_1\tau + iA_1(\omega_1 - \omega_{01})^2}, \quad (S18)$$

where  $\tau$  represents a relative time delay. The  $1/e$  temporal width of the chirped signal is

$$\Delta t = \frac{\sqrt{1 + 16A_1(1 - \rho_i^2)\sigma_1^4}}{2\sqrt{1 - \rho_i^2}\sigma_1} \quad (S19)$$

The escort pulse can be represented as a strong coherent state with a field as in (S9). The spectrum of the joint state after upconversion can be found as the convolution of the escort and the input signal spectra [27]

$$|F_f(\omega_3, \omega_h)| = \left| \int_{-\infty}^{\infty} d\omega_1 G(\omega_3 - \omega_1) \Phi_{SFG}(\omega_1, \omega_3 - \omega_1, \omega_3) F_i(\omega_1, \omega_h) \right| \quad (S20)$$

$$= \frac{1}{\sqrt{2\pi\sigma_3\sigma_{h,f}(1-\rho_i^2)^{1/4}}} \exp \left[ \frac{1}{1-\rho_f^2} \left( -\frac{(\omega_3 - \omega_{03})^2}{4\sigma_3^2} - \frac{(\omega_h - \omega_{0h,f})^2}{4\sigma_{h,f}^2} - \frac{\rho_f(\omega_3 - \omega_{03})(\omega_h - \omega_{0h,f})}{2\sigma_3\sigma_{h,f}} \right) \right], \quad (S21)$$

where we are able to re-express the state as a Gaussian since the convolution of two Gaussians is once again a Gaussian.

Even with Gaussian approximations to all the input functions, the theoretical final joint spectral intensity is difficult to express concisely. For the sake of intuition, we will look at its behaviour under various simplifications. First, we assume that phasematching is infinitely broad ( $\Phi_{SFG}(\omega_1, \omega_3 - \omega_1, \omega_3) \approx 1$ ). As we will see in Supplementary Section III, this assumption is not valid, but the phasematching is not so strong that it destroys the intuition gained from the simpler case. With this simplification, the spectral bandwidth  $\sigma_3$  of the output is

$$\sigma_3 = \sqrt{\frac{(2 - \rho_i^2)\sigma_1^2\sigma_e^2 + \sigma_e^4 + (1 - \rho_i^2)\sigma_1^4(1 + 16(A_1 + A_e)^2\sigma_e^4)}{\sigma_e^2 + (1 - \rho_i^2)\sigma_1^2(1 + 16A_1^2\sigma_1^2\sigma_e^2 + 16A_e^2\sigma_e^4)}} \quad (S22)$$

and the statistical correlation is

$$\begin{aligned} \rho_f = -\rho_i \frac{\sqrt{A_1^2(1 - \rho_i^2)\sigma_1^2 + A_e^2\sigma_e^2} \times \{1 + 16(A_1 + A_e)(1 - \rho_i^2)\sigma_1^2[(A_1 + 3A_e)(1 - \rho_i^2)\sigma_1^2 + A_e\sigma_e^2(1 + 16(A_1 + A_e)^2(1 - \rho_i^2)\sigma_1^4)]\}}{\sqrt{2}\sqrt{\sigma_e^2 + 2(1 - \rho_i^2)\sigma_1^2[1 + 8(A_1 + A_e)^2(1 - \rho_i^2)\sigma_1^2\sigma_e^2]}} \\ \times \frac{\sigma_e^2}{\{\sigma_e^2 + (1 - \rho_i^2)\sigma_1^2[1 + 16A_1^2(1 - \rho_i^2)\sigma_1^2\sigma_e^2 + 16A_e^2\sigma_e^4]\} \{(2 - \rho_i^2)\sigma_1^2\sigma_e^2 + \sigma_e^4 + (1 - \rho_i^2)\sigma_1^4[1 + 16(A_1 + A_e)^2\sigma_e^4]\}} \end{aligned} \quad (S23)$$

These expressions are difficult to parse without additional assumptions. Firstly, we look at the limit where the escort has infinite spectral support,  $\sigma_e \gg \sigma_1$ . As any chirp on a pulse with infinite spectral support stretches it infinitely, this is equivalent to the assumption that the chirped escort is much broader in time than the chirped signal if  $|A_e| \neq 0$ . In this limit, we find that the width of the upconverted signal is

$$\lim_{\sigma_e \rightarrow \infty} \sigma_3 = \frac{\sqrt{\frac{1}{1-\rho_i^2} + 16(A_1 + A_e)^2\sigma_1^4}}{4A_e\sigma_1} \stackrel{LCL}{=} \frac{|A_1 + A_e|\sigma_1}{A_e} = M_{\text{spectral}}\sigma_1, \quad (S24)$$

where  $M_{\text{spectral}} = 1/M_{\text{temporal}}$  is as defined in Eq. (2) of the main text, and the statistical correlation is

$$\lim_{\sigma_e \rightarrow \infty} \rho_f = -\rho_i \frac{4(A_1 + A_e)\sigma_1^2\sqrt{1 + 16(A_1 + A_e)^2(1 - \rho_i^2)^2\sigma_1^4}}{1 + 16(A_1 + A_e)^2(1 - \rho_i^2)\sigma_1^4} \stackrel{LCL}{=} -\rho_i \frac{A_1 + A_e}{|A_1 + A_e|} \quad (S25)$$

The simplification on the right-hand-side is once again the large-chirp limit (LCL), where we assume that  $16(A_1 + A_e)^2(1 - \rho_i^2)^2\sigma_1^4 \gg 1$ . We have also assumed that  $A_1 \neq -A_e$  in this simplification; if  $A_1 = -A_e$ , the process acts as a time-to-frequency converter, as described in Refs. [27, 29]. This simplification also relies on the initial state not being perfectly entangled,  $|\rho_i| < 1$ ,

as the marginal temporal length approaches infinity as the entanglement strengthens (consistent with being generated from truly-continuous-wave pumping). In this large chirp limit, the output waveform is recompressible through spectral phases without need for an additional time lens, and the joint spectrum maintains its degree of correlation.

In our experiment, the escort pulse has a bandwidth on the same order as that of the signal,  $\sigma_e \sim \sigma_1$ . We next focus on the case studied in our experiment, where  $A_e = -A_1/2$ . In the large-chirp limit of this scenario, the output width is

$$\sigma_3^{(M=-1)} \stackrel{LCL}{=} \frac{\sigma_1}{\sqrt{\frac{4\sigma_1^2}{\sigma_e^2} + 1}}, \quad (\text{S26})$$

and the statistical correlation is

$$\rho_f^{(M=-1)} \stackrel{LCL}{=} \frac{-\rho_i}{\sqrt{\frac{4(1-\rho_i^2)\sigma_1^2}{\sigma_e^2} + 1}}. \quad (\text{S27})$$

For both the bandwidth and correlation, the final value has the same absolute value as the input if the spectral support of the escort is sufficient,  $\sigma_e \gg 4\sigma_1(1 - \rho_i^2)$ . Additionally, the sign of the statistical correlation is reversed,  $\rho_f = -\rho_i$ , consistent with a magnification of -1. The deviations from this are due to lack of spectral support from the escort, and are exaggerated since the input signal is more strongly chirped than the escort; if the escort is not wider in frequency, it will be shorter in time when chirped and not encompass the full waveform [27]. In this case, the escort will act partially as a filter which will degrade the strength of entanglement in a Procrustean manner.

### III. TUNABILITY OF THE JOINT SPECTRUM

When a spatial lens is off-center relative to the incoming beam, the focus of the beam is translated, as in Fig. S-3a. Analogously, when a relative delay exists between the escort pulse and the input signal in an upconversion time lens, the central frequency of the upconverted signal will shift; a similar behaviour occurs in chirped-pulse bandwidth compression [29]. When we neglect the effects of limited escort bandwidth and restrictive phasematching (i.e.  $\sigma_e \rightarrow \infty$  and  $\Phi_{SG}(\omega_1, \omega_3 - \omega_1, \omega_3) \approx 1$ ) and take the large-chirp limit, the central frequency of the upconverted signal from an  $M = -1$  time lens can be found to be simply

$$\omega_{03}^{(ideal)} = \omega_{01} + \omega_{0e} + \frac{\tau}{A_1}, \quad (\text{S28})$$

where  $\tau$  is a relative delay applied to the signal,  $\omega_{01}$  and  $\omega_{0e}$  are the central frequencies of the input signal and escort pulse respectively, and  $A_1$  is the chirp on the input signal (the escort chirp  $A_e$  is assumed to be exactly  $-\frac{1}{2}A_1$ , as needed for  $M = -1$ ). The shift in herald center frequency,  $\delta\omega_{0h,f}$ , is zero in this limit.

However, once limited escort bandwidth and phasematching are taken into consideration, this approximation breaks down. The reasons for these discrepancies can be understood by looking at the phasematching and escort bandwidth. The effect of each of these imperfections is described graphically in Fig. S-3d. In the large-chirp limit, we can look at the limit where  $\sigma_e \ll \sigma_1$ , i.e. the escort is much narrower spectrally than the input signal. In this case, the chirped escort is much narrower in time than the chirped photon, and the upconversion acts as a filter, as shown in Fig. S-3c. The central frequency shifts are then

$$\lim_{\sigma_e \ll \sigma_1} \delta\omega_{03} \stackrel{LCL}{=} \frac{\tau}{2A_1} \quad (\text{S29})$$

$$\lim_{\sigma_e \ll \sigma_1} \delta\omega_{0h,f} \stackrel{LCL}{=} \frac{\rho\sigma_{h,i}\tau}{2A_1\sigma_1}. \quad (\text{S30})$$

		Upconverted signal tunability		Herald tunability	
Effective crystal length $L$	Effective escort bandwidth $\sigma_e$	$\delta\omega_{03}$	$\delta\lambda_{03}$	$\delta\omega_{0h}$	$\delta\lambda_{0h}$
Measured		0.86 THz/ps	0.071 nm/ps	-0.61 THz/ps	-0.18 nm/ps
$L_{meas.}$	$\sigma_{e,meas.}$	0.74 THz/ps	0.061 nm/ps	-0.74 THz/ps	-0.22 nm/ps
$0.65 \times L_{meas.}$	$\sigma_{e,meas.}$	0.86 THz/ps	0.071 nm/ps	-0.62 THz/ps	-0.18 nm/ps
0	$\infty$	1.45 THz/ps	0.121 nm/ps	0 THz/ps	0 nm/ps
0	$\sigma_{e,meas.}$	0.98 THz/ps	0.081 nm/ps	-0.50 THz/ps	-0.14 nm/ps
$L_{meas.}$	$\infty$	0.76 THz/ps	0.063 nm/ps	-0.72 THz/ps	-0.21 nm/ps

TABLE S-II. **Expected tunabilities with various assumptions.** The expected tunabilities of the central frequency for the upconverted signal and herald are given for a variety of assumptions, and can be compared with the tunabilities measured and shown in Fig. 3f. The experimental results are in agreement with the theory when the length is scaled to 65% of its physical value, likely due to the non-collinear geometry of the interaction. The ideal-world theory corresponds to where the phasematching is nonrestrictive ( $L = 0$ ) and the escort has infinite spectral support ( $\sigma_e \rightarrow \infty$ ). The experimental values are  $L_{meas.} = 1$  mm and  $\sigma_{e,meas.} = 7.38$  THz = 5.53 nm FWHM.

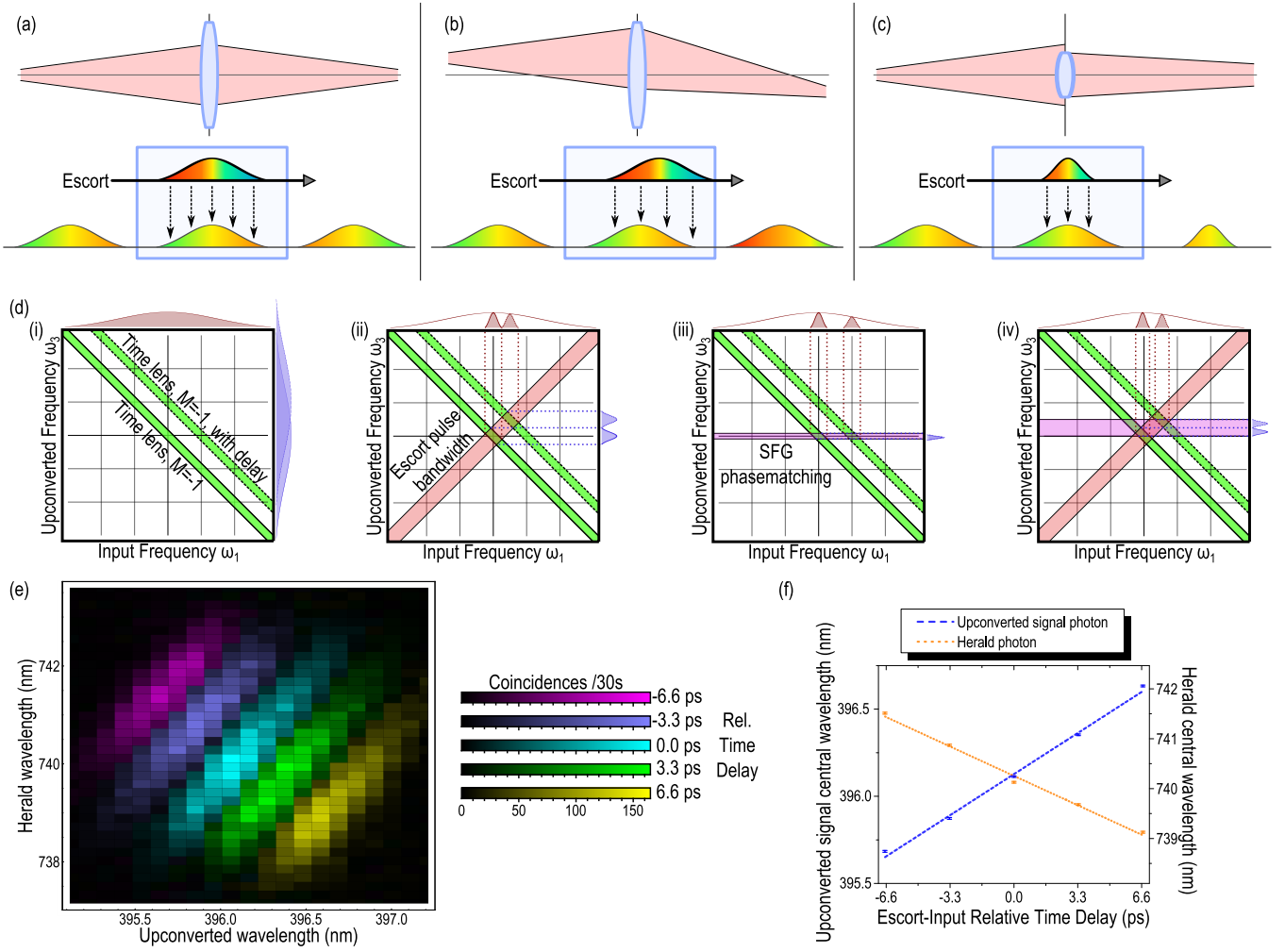


**Figure S-3. Joint spectrum tunability.** (a) The effect of the escort pulse on the signal in an upconversion time lens can be understood in analogy with the action of a lens in a spatial imaging system. (b) In an analogous fashion to how shifting the spatial center of a lens causes the deflection of a beam in space, a relative time delay on the escort pulse of an upconversion time lens causes a shift in the center frequency of the upconverted light. (c) If the spectral support of the escort pulse is limited, the upconverted light will have a narrower spectrum and longer temporal duration than the ideal scenario, analogous to a lens with limited clear aperture. (d) The reason both the output signal and herald central wavelengths may change can be understood by taking into account the effect of the chirp, finite escort bandwidth, and finite phasematching. The four plots shown give the mapping of an input frequency to an output frequency in the time-lens scenario; in the case where the input signal is frequency anti-correlated with a herald, the shift in the herald will be the opposite of the shift in the portion of the input signal accepted. (i) The chirps in the pulse, assuming a magnification of  $M = -1$ , flip an input frequency blue-shifted relative to its centre to one red-shifted of its new centre. Introducing a time delay effectively changes the centre, as can be visualized with two offset negatively sloped diagonal lines. In the absence of other effects, the input spectra is accepted in full, and thus the herald spectra will be unchanged when measured in coincidence. (ii) The sum-frequency process must conserve energy, and limiting the bandwidth of the escort pulse will enforce stricter conservation. If we consider the limit where the pulses are stretched well beyond their Fourier-limited widths by the chirp, this will result in the escort pulse acting as a filter, causing corresponding shifts in the signal and herald central frequencies when measured in coincidence. (iii) In the limit when the escort and input signal are degenerate in the sum-frequency process, the phasematching is roughly a restriction on the upconverted frequencies accessible. As changing the time delay changes which input frequency converts to a specific upconverted frequency, the herald spectrum may shift while the upconverted spectrum remains stable in this limit. (iv) As we see both central frequencies change as a function of delay but with difference slopes in terms of energy, we conclude that we observe a mixture of these competing effects. (e) Five measured joint spectra are shown with varied relative time delays between the escort pulse and input signal, reprinted from Fig. 3c of the main text. The shift in both the herald and output signal central wavelength is clearly apparent, but positive correlations are maintained throughout. (f) The fit upconverted (herald) central wavelength is seen to increase (decrease) as the relative delay is increased, with a best-fit slope of 0.071 nm/ps ( $-0.179$  nm/ps).

If  $\sigma_{h,i} \approx \sigma_1$  and the initial photon pair has strong frequency anti-correlations  $\rho_i \approx -1$ , the shift in each is simply opposite, which is due to selecting different parts of the input rather than upconverting the entire pulse.

We next look at the limit where the phasematching is restrictive. As we experimentally consider a sum-frequency process which is nearly degenerate between the escort and input signal, we make the approximation that the group velocities in the sum-frequency media of the two inputs are roughly equal. In this case, the phasematching function  $\Phi_{SG}(\omega_1, \omega_e, \omega_3) \approx \Phi_{SG}(\omega_3)$ , which we approximate to a Gaussian which grows tighter as the effective crystal length  $L$  is increased. In the large-chirp long-crystal limit, the upconverted signal is effectively untunable as phasematching restricts it to a specific output waveform, but the herald central frequency is found to be

$$\lim_{LCL} \lim_{L \rightarrow \infty} \delta\omega_{0h,f} = \frac{\rho\sigma_{h,i}\tau}{A_1\sigma_1}. \quad (\text{S31})$$

The herald changes since the phasematching only allows one frequency to be upconverted to, and the chirps applied force every interaction to be nearly monochromatic. Delaying the input signal changes which combination of frequencies from the escort and signal will combine to the accepted upconversion frequency, and will change which part of the input signal is upconverted.

We took five joint spectra as the delay between the escort and input signal was altered, as seen in Fig. S-3e, and saw a shift in both the herald and signal central frequencies, as seen in Fig. S-3f. Given our chirp parameter of  $A_1 = 696 \times 10^3 \text{fs}^2$ , we would expect a tunability of  $1.45 \frac{\text{THz}}{\text{ps}} = 0.12 \frac{\text{nm}}{\text{ps}}$  in an idealized case, but instead measure  $0.86 \frac{\text{THz}}{\text{ps}} = 0.071 \frac{\text{nm}}{\text{ps}}$ . The herald central frequency is also shifted, which would not occur ideally, with a slope of  $-0.61 \frac{\text{THz}}{\text{ps}} = 0.18 \frac{\text{nm}}{\text{ps}}$ . Our results are inconsistent with the idealized theory, as mentioned above, but are relatively consistent with a process modelled by the bandwidths we measured and a shortened effective crystal length, as seen in Table S-II. The shortened effective crystal length is expected as the signal photon and escort are combined non-collinearly in the upconversion medium and do not interact for the entire length of the crystal.

#### IV. DERIVATION AND BOUNDS ON THE NONLOCAL INTERFERENCE

The curves seen in Fig. 4 of the main text, often called Franson fringes [20], are a commonly used indicator of energy-time correlation in two-photon experiments. Here, we derive the expected fringe visibility without temporal filtering, which cannot be used to verify entanglement but can verify correlation independently of the joint spectrum.

In a scheme as visualized in Fig. S-4a, photons created from some source each go through either a long or short path in an unbalanced interferometer, with some phase. In our experiment, this delay was implemented by a birefringent crystal acting as a polarization-to-time converter and the phase by a series of waveplates, as seen in Fig. S-4b. If the difference between the two paths is longer than the coherence time of the individual photons, as given by the marginals of the joint spectrum, then we expect to see no interference in the single-detection events. However, if the time difference is less than the two-photon coherence time, then there will be interference in the coincidence detections. In the case where the photon pair is correlated in time (anti-correlated in frequency), this can be visualized as in Fig. S-4c, where the short-long and long-short paths are partially indistinguishable and interfere.

If the two-photon spectrum can be described in the Gaussian form with time delays  $\tau_i$  and phases in the long arm of  $\phi_i$  as

$$F(\omega_1, \omega_2) = \frac{1}{\sqrt{2\pi\sigma_1\sigma_2}(1-\rho^2)^{1/4}} \exp \left[ \frac{1}{1-\rho^2} \left( -\frac{(\omega_1 - \omega_{01})^2}{4\sigma_1^2} - \frac{(\omega_2 - \omega_{02})^2}{4\sigma_{h,i}^2} - \frac{\rho_i(\omega_1 - \omega_{01})(\omega_2 - \omega_{02})}{2\sigma_1\sigma_2} \right) \right] \quad (\text{S32})$$

$$\times \frac{1}{2}(1 + e^{-i\omega_1\tau_1 + i\phi_1})(1 + e^{-i\omega_2\tau_2 + i\phi_2}),$$

then the overall coincidence rate without spectral or temporal resolution can be found as

$$C(\phi_1, \phi_2) = \iint_{-\infty}^{\infty} d\omega_1 d\omega_2 |F(\omega_1, \omega_2)|^2 \quad (\text{S33})$$

$$\propto 1 + e^{-\sigma_1^2\tau_1^2} \cos \phi_1 + \frac{1}{2} e^{-\frac{1}{2}(\sigma_1^2\tau_1^2 - \rho\sigma_1\sigma_2\tau_1\tau_2 + \sigma_2^2\tau_2^2)} \cos(\phi_1 - \phi_2) \\ + \frac{1}{2} e^{-\frac{1}{2}(\sigma_1^2\tau_1^2 + \rho\sigma_1\sigma_2\tau_1\tau_2 + \sigma_2^2\tau_2^2)} \cos(\phi_1 + \phi_2) + e^{-\sigma_2^2\tau_2^2} \cos \phi_2 \quad (\text{S34})$$

For frequency anti-correlations ( $\rho < 0$ ), we expect to see nonlocal interference depending on  $\phi_1 + \phi_2$ ; for positive frequency correlations, we expect to see the interference dependent on  $\phi_1 - \phi_2$  instead. Note from Eq. (S33) that, without temporal selection, the coincidence rate is entirely dependent on the joint spectral *intensity*, not the field, and therefore gives no information on the temporal domain. With temporal filtering to eliminate unwanted coincidences, or with spectral resolution and frequency shifts replacing the time delays, it is possible to use this interference as a genuine measure of entanglement [20, 21]; as the time scales in our experiment were much smaller than detector resolution, this was unfortunately not an option. Since Eq. (S33) depends on the intensity rather than the field, the interference is independent of chirps and other applied dispersion. The single-detection events, on the other hand, have interference fringes described by

$$S_j(\phi_j) \propto 1 + e^{-\frac{1}{2}\sigma_j^2\tau_j^2} \cos \phi_j. \quad (\text{S35})$$



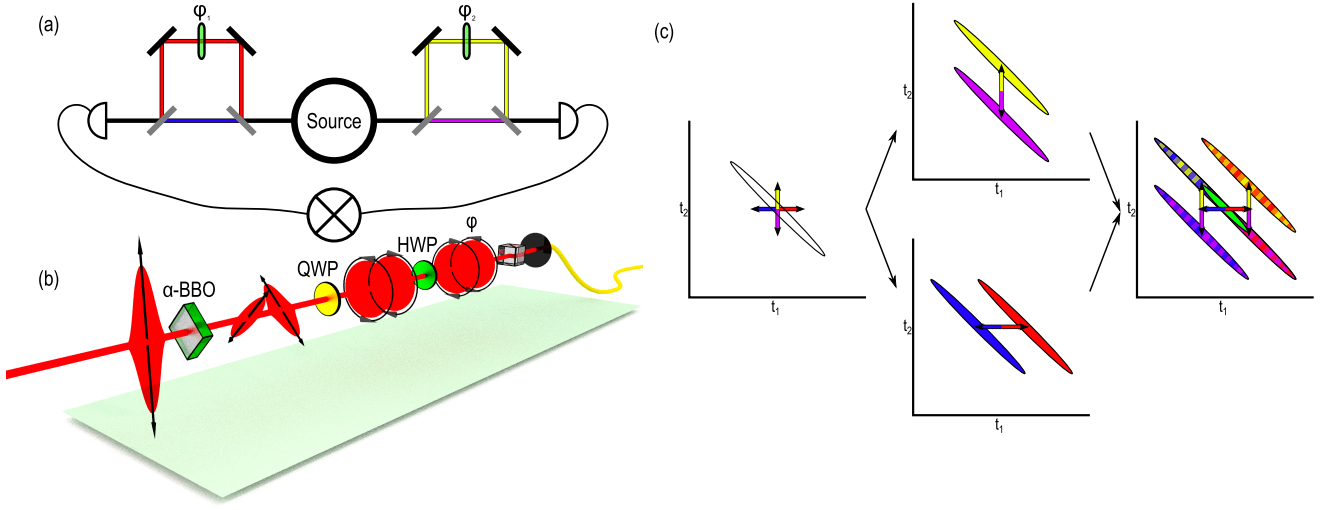


Figure S-4. **Nonlocal interference concept.** (a) Nonlocal interference fringes can be seen by sending each photon of a two-photon energy-time entangled pair through an unbalanced interferometer and altering the phase in one arm. In the ideal case, fringes should be visible in the coincidence measurements but not the single-detection events. (b) In our experiment, the unbalanced interferometer and phases are implemented through birefringent materials and wave-plates. A birefringent crystal splits a horizontally polarized photon into a diagonal portion and a delayed anti-diagonal portion. A quarter-wave plate converts diagonal and anti-diagonal to left- and right-circularly polarized light. A half-wave plate then introduces a phase between the circularly polarized photons. The polarization information is then erased with a polarizing beamsplitter. (c) When the state is anti-correlated in time (positive spectral correlations), the interference is between the semi-indistinguishable late-early and early-late paths (blue-yellow and red-magenta). The visibility should be proportional to their overlap, visualized in green.

While we cannot use the interference observed to verify entanglement, we can use it to verify correlation independently of the joint spectral analysis. Generally, an interference fringe can be represented as  $a(1 + V \cos \theta)$ , where  $\theta$  is a hidden variable which may depend on some hidden distribution. The visibility, defined as  $V = \frac{\max - \min}{\max + \min}$ , of two-site uncorrelated interference is limited to  $V_{\text{uncorr}} = \frac{V_1 + V_2}{1 + V_1 V_2}$ . In the limit of no entanglement ( $\rho = 0$ ), Eq. (S34) simplifies to this. To show correlation, we simply need to show a visibility greater than  $V_{\text{uncorr}}$ . Using the data displayed in Fig. 4b-c of the main text, we fit each slice (i.e. holding either  $\phi_{\text{up}}$  or  $\phi_{\text{her}}$  constant) to a sinusoid and find an average visibility in the coincidence counts of  $(15.6 \pm 1.0)\%$ , which increases to  $(17.5 \pm 1.2)\%$  when the background is subtracted. The upconverted singles have a visibility of only  $(0.4 \pm 0.4)\%$ , or  $(0.9 \pm 0.5)\%$  when background subtracted, and the herald singles have a visibility of just  $(0.06 \pm 0.04)\%$ . Using these visibilities, we find that  $V_C - V_{\text{uncorr}} = (15.2 \pm 1.1)\%$  or  $(16.6 \pm 1.3)\%$  background subtracted, more than 13 standard deviations above uncorrelated in either case. Additionally, the fringes of Fig. 4b display the expected  $\cos(\phi_1 - \phi_2)$  dependence of positive frequency correlations.